High-pressure structural configuration and phase transition in celsian, BaAl2Si2O8

Phys Chem Minerals
DOI 10.1007/s00269-016-0847-0

ORIGINAL PAPER

High-pressure structural configuration and phase transition in celsian, $BaAl_2Si_2O_8$

Nadia Curetti[1,2] · **Piera Benna**[1,2] · **Emiliano Bruno**[1,2]

Received: 10 July 2016 / Accepted: 22 September 2016

Abstract In situ high-pressure X-ray diffraction study was performed on celsian ($Cls_{97}Or_3$) from Jakobsberg, Sweden. A single crystal of celsian was loaded in an ETH-type diamond anvil cell, and unit-cell parameters were measured at 20 different pressures up to 6.0 GPa at room *T*. The evolution of the unit-cell parameters and volume as a function of pressure shows a discontinuity at $P \sim 5.7$ GPa indicating a displacive first-order phase transition. The *P*–*V* data were fitted by a second-order Birch–Murnaghan EoS only up to 2.55 GPa, because at higher pressures a slight change in the compressional behavior of the unit-cell volume is observed, indicating a pre-transition volume softening. The resulting EoS coefficients are $V_0 = 1461.4(1)$ Å^3 and $K_{T0} = 88.1(6)$ GPa. A second crystal of celsian was loaded in the DAC cell, and single-crystal in situ H*P* X-ray diffraction was performed at $P = 0.0001$, 2.1, 4.2, 5.5, 5.9, 6.5 and 7.8 GPa. The data collections between 0 and 5.5 GPa show only *a*- and *b*-type reflections confirming the *I*2/*c* space group. The appearance of *c* and *d*-type reflections at 5.9, 6.5 and 7.8 GPa, the analysis of the systematic absence and the structural refinements define the H*P* phase transition as an *I*2/*c*–*P*2$_1$/*c* transition. The most significant changes with compression in celsian are the deformation in the Ba polyhedra and the variation in the T–O–T angles.

Keywords Crystal structure · High-pressure studies · Celsian · Equation of state · Phase transition

Introduction

Barium feldspar, celsian (formula: $BaAl_2Si_2O_8$, symbol: Cls, space group: *I*2/*c*), belongs to the alkaline-earth feldspar with Al:Si ratio equal to 1:1 and contains the heaviest cation normally found in feldspars. Newnham and Megaw (1960) determined the structure at room condition of a celsian from Broken Hill, Australia, containing an appreciable amount of K ($Cls_{\sim 84}Or_{\sim 18}$), using Fourier difference maps and least squares methods. The authors observed that the Al, Si distribution among the tetrahedral sites is partially ordered ("each predominantly aluminum tetrahedron is surrounded by four predominantly silicon tetrahedra, and vice versa") and that the Ba atom influences the surrounding silicate framework. Ba atom is ninefold coordinated, with an irregular configuration very similar to that of K in sanidine or microcline, but the Ba–O distances are nearly all shorter, particularly for oxygens $O_A(2)$ and O_B. Moreover, the Ba atom has a marked anisotropic temperature factor with the shortest axis of the vibration ellipsoid close to **a***. The structure refinement conducted by Griffen and Ribbe (1976) in nearly pure celsian ($Cls_{95}Or_5$) from Jakobsberg, Sweden, confirms the results of Newnham and Megaw (1960) "particularly with regard to the tetrahedral O···O distances, O–T–O angles, and mean T–O and Ba, K–O bond lengths," despite the difference in chemical composition.

The aim of the present work is to investigate the high-pressure behavior of celsian and to detail the possible presence of phase transitions, in order to contribute to the

Electronic supplementary material The online version of this article (doi:10.1007/s00269-016-0847-0) contains supplementary material, which is available to authorized users.

✉ Piera Benna
piera.benna@unito.it

[1] Dipartimento di Scienze della Terra, Università degli Studi di Torino, Via Valperga Caluso 35, 10125 Turin, Italy

[2] CrisDi Interdepartmental Center for Crystallography, Università degli Studi di Torino, Via P. Giuria 5, 10125 Turin, Italy

Published online: 07 October 2016

knowledge of structural evolution of feldspars at H*P*. Recent study performed on natural and synthetic feldspars reveals several complexities at high pressures as "elastic softening and completely new symmetries and sequences of phase transformations" (Nestola et al. 2008). While in the alkali feldspars ($AlSi_3$ feldspars) investigated at H*P* no phase transitions were observed (Downs et al. 1994; Allan and Angel 1997; Nestola et al. 2008; Curetti et al. 2011), in Al_2Si_2 feldspars several pressure-induced phase transitions have been found. The Val Pasmeda anorthite (macroscopic order parameter $Q_{od} = 0.92$) shows a reversible first-order $P\bar{1}$–$I\bar{1}$ phase transition between 2.6 and 2.7 GPa (Angel et al. 1988; Angel 1988, 1992). With increasing disorder ($Q_{od} = 0.78$), the transition becomes continuous in character and there is an increase in the pressure of the transition ($P_T = 4.8$ GPa) (Angel 1992). In the synthetic $Ca_{0.2}Sr_{0.8}Al_2Si_2O_8$ feldspar ($An_{20}SrFsp_{80}$), triclinic at room temperature, Nestola et al. (2004) and Benna et al. (2007) observed at $P \sim 4.3$ GPa a first-order $I\bar{1}$–$I2/c$ transformation, and a further transition at $P \sim 7.3$ GPa, strongly first order, to the $P2_1/c$ space group, never observed in feldspars until then. Recently, Pandolfo et al. (2011) found in synthetic strontium feldspar ($SrAl_2Si_2O_8$) the same first-order $I2/c$ to $P2_1/c$ transition at $P = 6.6$ GPa. Curetti et al. (2015) observe the $I2/c$–$P2_1/c$ transition in synthetic lead feldspar ($PbAl_2Si_2O_8$) at $P \sim 8$ GPa.

Experimental methods

The nearly pure celsian ($Cls_{97}Or_3$) (formula: $Ba_{0.97}K_{0.03}Al_{1.95}Si_{2.04}O_8$) studied in this work, comes from Jakobsberg, Sweden. A single crystal of celsian of size $120 \times 80 \times 50$ μm^3 was selected on the base of its optical features and loaded in an ETH-type diamond anvil cell (DAC, hereafter) (Miletich et al. 2000). A foil of T301 steel 250 μm thick was used as a gasket to hold the crystal, and it was pre-indented to 110 μm before drilling a hole by spark erosion (∅ 250 μm). A 16:3:1 mixture of methanol:ethanol:water was used as hydrostatic pressure-transmitting medium. The internal pressure and the uncertainty on *P* were calculated by using a crystal of quartz as standard internal (using 12 reflections) (Angel et al. 1997). The unit-cell parameters were determined at room *T* in the *P* range 0.0001–6.0 GPa from the setting angles of 27 reflections centered in eight positions (King and Finger 1979; Angel et al. 2000), using a Siemens P4 four-circle X-ray diffractometer equipped with point detector (Mo*K*α radiation; Department of Earth Sciences, University of Torino) and with the SINGLE Control Program software (Angel and Finger 2011). The unit-cell parameters were measured at overall 20 different pressures and are reported in Table 1.

Table 1 Unit-cell parameters of celsian as a function of pressure (esd in brackets)

P (GPa)	*a* (Å)	*b* (Å)	*c* (Å)	*β* (°)	*V* (Å^3)
0.0001[a]	8.615(6)	13.0312(16)	14.377(2)	115.13(2)	1461(1)
0.0001	8.615(8)	13.031(2)	14.376(4)	115.10(3)	1461(2)
0.26(2)	8.604(4)	13.0199(12)	14.3673(17)	115.124(15)	1457(1)
0.38(2)	8.599(4)	13.0153(12)	14.3614(18)	115.128(16)	1455(1)
1.10(2)	8.569(4)	12.9875(13)	14.3226(19)	115.119(17)	1443(1)
1.36(2)	8.559(4)	12.9807(12)	14.3117(18)	115.114(16)	1440(1)
1.70(3)	8.546(4)	12.9683(11)	14.2946(17)	115.103(15)	1435(1)
2.16(3)	8.526(4)	12.9508(13)	14.2726(19)	115.091(18)	1427(1)
2.55(3)	8.512(3)	12.9403(9)	14.2579(13)	115.101(11)	1422(1)
2.79(3)	8.494(4)	12.9287(14)	14.243(2)	115.106(18)	1416(1)
3.13(3)	8.474(4)	12.9170(11)	14.2220(16)	115.080(15)	1410(1)
3.44(3)	8.463(3)	12.9049(10)	14.2051(15)	115.047(14)	1405(1)
3.80(3)	8.438(4)	12.8851(13)	14.1760(19)	114.989(17)	1397(1)
3.94(5)	8.426(3)	12.8778(10)	14.1647(14)	114.973(13)	1393(1)
4.33(2)	8.413(3)	12.8615(12)	14.1422(15)	114.912(14)	1388(1)
4.67(6)	8.391(4)	12.8463(14)	14.1163(18)	114.857(16)	1381(1)
5.05(5)	8.369(4)	12.8264(15)	14.0858(18)	114.832(17)	1372(1)
5.18(5)	8.364(4)	12.8238(13)	14.0808(17)	114.815(15)	1371(1)
5.59(5)	8.343(5)	12.8023(19)	14.053(2)	114.78(2)	1363(1)
5.90(6)[b]	8.315(8)	12.707(3)	14.023(4)	114.36(4)	1350(2)
6.01(4)[b]	8.315(8)	12.705(3)	14.012(4)	114.32(4)	1349(1)

[b] $P2_1/c$ space group

[a] In air

Table 2 Single-crystal data at different pressures

P (GPa)	0.0001[a]	2.1	4.2	5.5	5.9	6.5	7.8
Space group	*I*2/*c*	*I*2/*c*	*I*2/*c*	*I*2/*c*	$P2_1/c$	$P2_1/c$	$P2_1/c$
a (Å)	8.628(9)	8.527(3)	8.422(3)	8.363(3)	8.3414(7)	8.313(3)	8.2791(19)
b (Å)	13.0380(10)	12.9449(5)	12.8618(4)	12.8089(4)	12.7458(3)	12.6714(4)	12.5505(3)
c (Å)	14.44(4)	14.312(13)	14.169(11)	14.114(13)	14.0574(16)	13.994(12)	13.896(9)
β (°)	115.1(2)	114.98(8)	114.89(7)	114.75(7)	114.383(10)	114.13(8)	113.78(5)
V (Å^3)	1471(4)	1432.0(14)	1392.3(12)	1373.0(14)	1361.2(2)	1345.3(13)	1321.3(9)
Refl. unique	599	435	626	607	1048	1250	1069
Refl. a $F_o \geq 1\sigma(F_o)$	324	293	376	370	267	339	283
Refl. b $F_o \geq 1\sigma(F_o)$	275	142	250	237	257	289	249
Refl. c $F_o \geq 1\sigma(F_o)$	–	–	–	–	244	289	256
Refl. d $F_o \geq 1\sigma(F_o)$	–	–	–	–	280	333	281
Refl. $F_0 \geq 4\sigma(F_0)$	471	362	549	529	622	985	849
R (%) $F_0 \geq 1\sigma(F_0)$	9.60	5.74	9.28	8.54	12.33	10.73	13.11
R (%) $F_0 \geq 4\sigma(F_0)$	7.23	4.17	6.66	6.64	5.92	7.65	8.14
Weight	0.24	0.14	0.16	0.21	0.18	0.23	0.24
Goodness of fit	1.21	1.07	1.21	1.14	1.05	1.18	1.15

[a] Within the DAC

$W = 1/[\sigma^2(F_0^2) + (a \cdot P)^2]$, where $P = (F_0^2 + 2F_c^2)/3$

Another crystal of celsian of the same locality was selected (size 110 × 90 × 50 μm^3) for single-crystal structure determinations at high pressure. A preliminary characterization at room conditions was performed using a Siemens P4 four-circle X-ray diffractometer, equipped with point detector, graphite-monochromatized Mo*K*α radiation, θ–2θ scan mode, variable scanning speed (2.4–30°/min). An empirical absorption correction, based on the ψ-scan method (North et al. 1968), was used. A total of 4632 reflections were measured, of with 2141 unique. The data collection shows only *a* ($h + k$ = even, l = even) and *b*-type ($h + k$ = odd, l = odd) reflections, confirming the *I*2/c space group as in Newnham and Megaw (1960). Unit-cell parameters at room conditions are a = 8.630(1), b = 13.043(2), c = 14.403(2) Å, β = 115.19(1)°, V = 1467(1) Å^3. The structural data were refined starting from the fractional coordinates of Griffen and Ribbe (1976) and using the neutral atomic scattering factor of the Ba, Si, Al and O. Structural details were refined using SHELX-97 package (Sheldrick 2008). The anisotropic refinement of 120 parameters converges at R = 3.25 % for 1353 reflections with $Fo \geq 4\sigma(Fo)$ and R = 5.63 % for all 2141 data. With $F_o \geq 1\sigma(F_o)$, the number of *a* and *b* reflections observed is 1109 and 1032, respectively. The Q_{od} parameter, calculated from ⟨T–O⟩ bond lengths following Angel et al. (1990), is 0.86 and indicates an order degree higher than that obtained by previous authors. Afterward the room T characterization, the sample was loaded in the DAC cell in order to investigate the structural changes with increasing pressure. The internal pressure was checked with Horiba-Jomin Micro-Raman spectrometer (Scansetti Interdepartmental Centre, University of Torino) by the shift of the fluorescence lines of five rubies (Ø 15 μm) as standard internal (Mao et al. 1986). Single-crystal diffraction intensities were collected with a Gemini R Ultra X-ray diffractometer equipped with a Ruby CCD detector, using monochromatic Mo*K*α radiation and the tube operating at 50 kV and 40 mA (CrisDi Interdepartmental Center, University of Torino) at P = 0.0001, 2.1, 4.2, 5.5, 5.9, 6.5 and 7.8 GPa. A total of 16 runs with 1783 frames were collected (frame width 0.2°, exposure time 50 s, sample–detector distance 82 mm), covering the whole accessible reciprocal space. The 171.37.35 version of CrysAlisPro software (Agilent Technologies) was used to integrate the intensity data and for analytical absorption and Lorentz-polarization correction. Integrated intensities were corrected for the absorption of the DAC cell and for the gasket shadow using ABSORB-7 software (Angel and Gonzalez-Platas 2013). Unit-cell parameters at room conditions are a = 8.628(9), b = 13.0380(10), c = 14.44(2) Å, β = 115.1(2)°, V = 1471(4) Å^3 (Table 2). Structural details were refined using SHELX-97 package (Sheldrick 2008). The measurements at room pressure and at P = 2.1, 4.2, 5.5 GPa showed only *a*- and *b*-type reflections confirming the *I*2/c space group. At P = 5.9, 6.5 and 7.8 GPa, the data collection also showed the presence of *c* ($h + k$ = even, l = odd) and *d*-type reflections ($h + k$ = odd, l = even) indicating a primitive lattice.

Table 3 Atomic fractional coordinates and displacement parameters (Å^2) for *I*2/*c* celsian at different pressures

P (GPa)	Site	*x*	*y*	*z*	U_{iso}/U^a_{eq}	Site	*x*	*y*	*z*	U_{iso}
0.0001	Ba	0.2825(2)	0.0001(1)	0.0652(2)	0.0494(18)					
2.1		0.2813(1)	0.0003(1)	0.0663(2)	0.0278(15)					
4.2		0.2795(2)	0.0007(1)	0.0686(2)	0.0292(17)					
5.5		0.2796(2)	0.0009(1)	0.0708(3)	0.038(2)					
0.0001	$T_1(0)$	0.0120(8)	0.1810(2)	0.1119(9)	0.0094(8)	$T_1(z)$	0.0108(9)	0.1835(3)	0.6215(10)	0.0109(9)
2.1		0.0081(8)	0.1821(2)	0.1091(9)	0.0095(8)		0.0036(9)	0.1844(2)	0.6158(11)	0.0090(10)
4.2		0.0027(10)	0.1830(3)	0.1064(11)	0.0142(8)		−0.0021(11)	0.1853(3)	0.6140(13)	0.0154(10)
5.5		0.0013(10)	0.1838(3)	0.1079(12)	0.0172(9)		−0.0046(11)	0.1858(3)	0.6139(13)	0.0183(10)
0.0001	$T_2(0)$	0.7047(10)	0.1219(3)	0.1694(11)	0.0107(9)	$T_2(z)$	0.6958(9)	0.1151(3)	0.6696(10)	0.0116(8)
2.1		0.7068(10)	0.1234(3)	0.1758(11)	0.0096(9)		0.6984(9)	0.1148(2)	0.6768(10)	0.0091(7)
4.2		0.7002(12)	0.1240(3)	0.1728(14)	0.0129(10)		0.6899(10)	0.1153(3)	0.6717(11)	0.0124(8)
5.5		0.7009(11)	0.1242(3)	0.1752(13)	0.0147(10)		0.6910(10)	0.1148(3)	0.6752(12)	0.0135(9)
0.0001	$O_A(1)$	0.0054(19)	0.1370(8)	0.002(2)	0.016(2)	$O_A(2)$	0.621(2)	0.0006(5)	0.144(2)	0.0085(18)
2.1		0.002(2)	0.1381(6)	0.000(2)	0.0141(16)		0.6171(19)	0.0003(6)	0.145(2)	0.0124(15)
4.2		0.006(3)	0.1387(7)	0.002(3)	0.018(2)		0.612(2)	0.0004(7)	0.147(3)	0.0141(18)
5.5		0.003(2)	0.1397(7)	0.000(3)	0.0109(19)		0.617(2)	0.0009(6)	0.159(3)	0.014(2)
0.0001	$O_B(0)$	0.833(2)	0.1385(7)	0.105(2)	0.015(2)	$O_B(z)$	0.816(2)	0.1379(7)	0.613(3)	0.019(2)
2.1		0.835(2)	0.1357(6)	0.110(2)	0.016(2)		0.815(2)	0.1368(6)	0.615(2)	0.018(2)
4.2		0.831(3)	0.1348(9)	0.110(3)	0.031(3)		0.803(3)	0.1351(9)	0.609(3)	0.028(3)
5.5		0.824(3)	0.1349(11)	0.104(3)	0.035(3)		0.805(3)	0.1340(11)	0.612(4)	0.040(4)
0.0001	$O_C(0)$	0.022(2)	0.3046(7)	0.118(2)	0.013(2)	$O_C(z)$	0.027(2)	0.3151(6)	0.628(2)	0.0097(18)
2.1		0.018(2)	0.3045(6)	0.122(2)	0.011(2)		0.023(2)	0.3152(6)	0.634(2)	0.012(2)
4.2		0.004(3)	0.3063(8)	0.117(3)	0.022(3)		0.019(3)	0.3178(7)	0.635(3)	0.017(2)
5.5		0.005(3)	0.3067(9)	0.121(4)	0.031(3)		0.015(3)	0.3172(8)	0.636(3)	0.025(3)
0.0001	$O_D(0)$	0.187(2)	0.1301(7)	0.198(3)	0.015(2)	$O_D(z)$	0.1977(19)	0.1204(6)	0.708(2)	0.0087(18)
2.1		0.180(3)	0.1325(7)	0.191(3)	0.019(2)		0.188(3)	0.1225(7)	0.699(3)	0.017(2)
4.2		0.186(3)	0.1356(9)	0.199(4)	0.025(3)		0.192(3)	0.1236(7)	0.705(3)	0.015(2)
5.5		0.179(4)	0.1381(10)	0.195(5)	0.034(3)		0.188(4)	0.1265(10)	0.704(4)	0.029(3)

All atoms except for Ba were refined with isotropic displacement parameters

The isotropic displacement exponent takes the form: $-8\pi^2 U(\sin\theta/\lambda)^2$

[a] U_{eq} defined as one third of the trace of the orthogonalized U_{ij} tensor

Only reflections *h*0*l*, 00*l* and 0*k*0 with *l* and *k* even were observed, indicating the presence of a screw axis along the *b* direction. Therefore, the analysis of the systematic absences confirms the $P2_1/c$ symmetry at $P = 5.9$, 6.5 and 7.8 GPa. In the $P2_1/c$ refinements, all the atoms of *I*2/*c* symmetry were splitted in two non-equivalent sites taking into account the change of origin by ¼, ¼, ¼ in the $P2_1/c$ space group. For all the refinements, anisotropic displacement parameters were introduced only for extra-framework Ba cations. Unit-cell parameters and refinements details at different pressures are reported in Table 2. Fractional atomic coordinates and displacement parameters are listed in Tables 3 (*I*2/*c* space group) and 4 ($P2_1/c$ space group) (CIF files deposited of Electronic supplementary material).

Results and discussion

Elastic behavior and equation of state

The unit-cell parameters of celsian up to $P = 6$ GPa are reported in Table 1, and the evolutions of the unit-cell parameters and volume with pressure are shown in Figs. 1 and 2, respectively. A discontinuity is visible at ~5.7 GPa, indicating a first-order phase transition. The discontinuous character of the transition is especially noticeable in the *b* and β plots.

In the *P* range 0.0001–5.59 GPa, the *a*, *b* and *c* linear parameters decrease with increasing pressure (Fig. 1) and show a negative axial variation by 3.2, 1.8 and 2.2 %, respectively. The axial compressibilities, calculated with

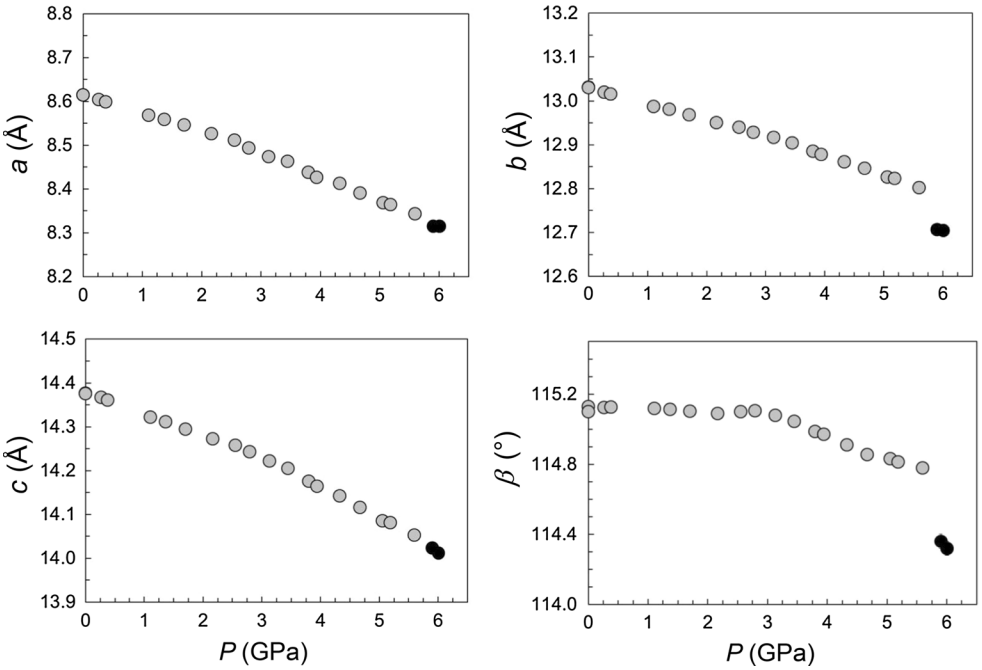

Fig. 1 Variation of the *a*, *b*, *c* and β unit-cell parameters with pressure in celsian. *Gray circles*: *I*2/*c* phase. *Black circles*: $P2_1/c$ high-pressure phase. Experimental uncertainties are smaller than *symbols*

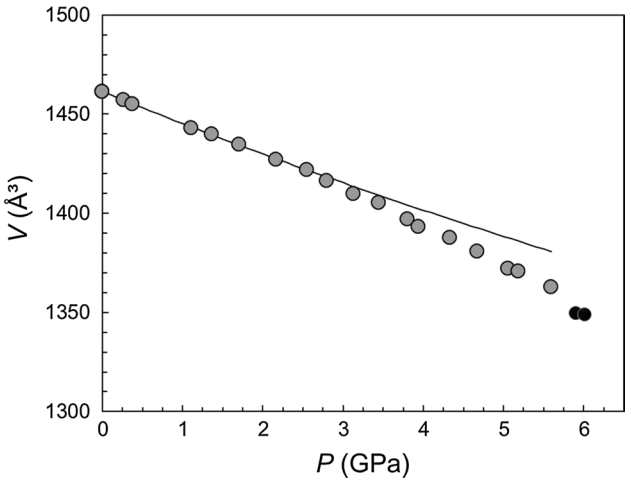

Fig. 2 Evolution of the unit-cell volume as a function of pressure for celsian. *Symbols* as in Fig. 1. *Solid line* shows the second-order Birch–Murnaghan equation of state (BM2-EoS) in the *P* range 0.0001–2.55 GPa. Experimental uncertainties are smaller than *symbols*

the formula $\beta = -(d - d_0)/d_0 \times 1/P$ (where *d* is a unit-cell parameter), are reported in Table 5, in order to compare them with the linear compressibilities of the other monoclinic Al_2Si_2 feldspars investigated at H*P*. In celsian, the axial compressibilities ($\beta a = 5.65$, $\beta b = 3.14$, $\beta c = 4.02 \times 10^{-3}$ GPa^{-1}) show the typical trend previously observed in feldspars: $\beta a > \beta c > \beta b$ (Angel et al. 1988), with the *a* axis as the most compressible. The axial anisotropy ($\Delta a/a_0$:$\Delta b/b_0$:$\Delta c/c_0$ = 1.8:1:1.3) is quite similar to that of lead feldspar, and it is higher than monoclinic *I*2/*c* $An_{20}SrFsp_{80}$ feldspar and $SrFsp_{100}$ feldspar, but lower than that observed in overall alkali feldspars studied at H*P* (Nestola et al. 2008). Closer inspection of the variation of the unit-cell parameters of celsian with pressure is done using the normalized plots (Fig. 3). The figure indicates that the linear parameters show normal compressional behavior up to 2.55 GPa (*gray symbols* in Fig. 3), with the *a* axis significantly softer than the *b* or *c* axes, but at higher pressures all the axes appear to become relatively softer. Therefore, the compressibilities of unit-cell axes were determined by fitting a second-order Birch–Murnaghan Equation of State (BM2-EoS) to a, *b* and *c* parameters (*solid lines* in Fig. 3) only up to 2.55 GPa, using the EosFit7c/EosFit7-GUI softwares (Angel et al. 2014). The coefficients obtained are: $a_0 = 8.6153(4)$ Å, 1/3 $M_0 = 65.7(4)$ GPa; $b_0 = 13.0301(7)$ Å, 1/3 $M_0 = 115.5(1.6)$ GPa; $c_0 = 14.3781(10)$ Å, 1/3 $M_0 = 94.9(1.4)$ GPa (with $M_i = \beta_i^{-1}$, Angel et al. 2014). The anomalous compressional pattern, at *P* higher than 2.55 GPa, indicates a pre-transition elastic softening, typically associated with first-order transitions (Miletich et al. 2014).

As regards the β angle evolution with pressure, in celsian it does not change up to 3 GPa (Fig. 1) and then slightly decreases. In the other Al_2Si_2 feldspars, the β angle decreases with pressure (Angel et al. 1988; Tribaudino et al. 1999; Benna et al. 2007; Pandolfo et al. 2011; Curetti et al. 2015) while it increases in alkali feldspars with a plateau effect (Allan and Angel 1997; Nestola et al. 2008).

In order to compare celsian with the other monoclinic feldspars compressed at H*P*, the strain induced by increasing pressure has been evaluated from the unit-cell

Table 4 Atomic fractional coordinates and displacement parameters (Å^2) for $P2_1/c$ celsian at different pressures

P (GPa)	Site	x	y	z	U_{iso}/U^a_{eq}	Site	x	y	z	U_{iso}/U^a_{eq}
5.9	Ba(0)	0.2885(2)	0.0029(1)	0.0638(3)	0.0309(15)	Ba(i)	0.7719(2)	0.4991(1)	0.5766(2)	0.0179(14)
6.5		0.2900(3)	0.0037(1)	0.0637(3)	0.050(2)		0.7717(3)	0.4983(1)	0.5762(3)	0.045(2)
7.8		0.2908(3)	0.0047(1)	0.0630(4)	0.044(2)		0.7720(3)	0.4966(1)	0.5741(4)	0.048(2)
5.9	T_1(00)	0.0029(9)	0.1782(3)	0.1104(10)	0.0089(8)	T_1(0i)	0.4919(9)	0.6920(3)	0.6006(11)	0.0107(9)
6.5		0.0037(12)	0.1781(3)	0.1124(12)	0.0116(9)		0.4880(12)	0.6933(3)	0.5979(13)	0.0130(9)
7.8		0.0037(12)	0.1785(4)	0.1148(15)	0.0131(11)		0.4843(12)	0.6955(4)	0.5955(15)	0.0143(11)
5.9	T_1(z0)	0.0001(10)	0.1759(3)	0.6180(12)	0.0106(9)	T_1(zi)	0.4903(10)	0.6963(3)	0.1100(11)	0.0093(9)
6.5		0.0022(13)	0.1741(3)	0.6223(14)	0.0122(10)		0.4896(13)	0.6982(3)	0.1074(13)	0.0120(10)
7.8		0.0007(13)	0.1722(4)	0.6215(16)	0.0125(12)		0.4925(12)	0.7014(4)	0.1097(15)	0.0125(12)
5.9	T_2(00)	0.7023(11)	0.1293(3)	0.1770(12)	0.0110(10)	T_2(0i)	0.1948(11)	0.6222(3)	0.6730(12)	0.0088(10)
6.5		0.7004(14)	0.1311(4)	0.1788(15)	0.0150(11)		0.1989(13)	0.6218(3)	0.6787(13)	0.0073(10)
7.8		0.7029(15)	0.1362(5)	0.1841(18)	0.0170(14)		0.1943(14)	0.6217(4)	0.6756(17)	0.0122(12)
5.9	T_2(z0)	0.6934(10)	0.1110(3)	0.6753(11)	0.0102(8)	T_2(zi)	0.1866(10)	0.6187(3)	0.1751(11)	0.0104(9)
6.5		0.6968(12)	0.1082(3)	0.6794(13)	0.0121(10)		0.1860(13)	0.6194(3)	0.1755(13)	0.0099(10)
7.8		0.6991(12)	0.1050(4)	0.6839(15)	0.0130(11)		0.1846(11)	0.6212(4)	0.1761(14)	0.0103(10)
5.9	O_A(10)	0.002(2)	0.1431(8)	−0.004(3)	0.017(3)	O_A(1i)	0.502(2)	0.6391(7)	0.502(3)	0.011(2)
6.5		0.007(3)	0.1433(9)	−0.001(4)	0.016(3)		0.500(3)	0.6379(10)	0.501(3)	0.017(3)
7.8		0.010(3)	0.1431(11)	0.004(4)	0.016(3)		0.494(3)	0.6350(12)	0.490(4)	0.020(3)
5.9	O_A(20)	0.624(2)	0.0054(6)	0.183(3)	0.014(2)	O_A(2i)	0.110(2)	0.4976(6)	0.641(3)	0.0099(19)
6.5		0.631(3)	0.0071(7)	0.194(3)	0.010(2)		0.102(3)	0.4975(7)	0.626(3)	0.013(2)
7.8		0.640(3)	0.0119(9)	0.212(3)	0.010(2)		0.116(3)	0.4954(10)	0.639(4)	0.016(3)
5.9	O_B(00)	0.827(3)	0.1254(7)	0.107(3)	0.013(2)	O_B(0i)	0.326(3)	0.6431(8)	0.613(3)	0.022(3)
6.5		0.823(4)	0.1243(10)	0.105(4)	0.023(3)		0.316(4)	0.6453(10)	0.605(4)	0.026(3)
7.8		0.830(4)	0.1226(12)	0.113(5)	0.025(4)		0.306(4)	0.6518(12)	0.601(4)	0.023(4)
5.9	O_B(z0)	0.812(3)	0.1161(8)	0.618(3)	0.020(3)	O_B(zi)	0.293(3)	0.6492(8)	0.102(3)	0.021(3)
6.5		0.805(3)	0.1095(9)	0.605(3)	0.020(3)		0.299(4)	0.6531(9)	0.114(4)	0.024(3)
7.8		0.816(3)	0.1043(11)	0.615(4)	0.020(3)		0.299(3)	0.6581(11)	0.114(4)	0.017(3)
5.9	O_C(00)	0.003(2)	0.3022(7)	0.127(3)	0.015(2)	O_C(0i)	0.493(2)	0.8154(6)	0.600(3)	0.011(2)
6.5		–0.003(3)	0.3043(9)	0.125(3)	0.021(3)		0.497(3)	0.8199(8)	0.605(3)	0.014(2)
7.8		0.005(3)	0.3059(11)	0.140(4)	0.018(3)		0.493(3)	0.8218(11)	0.598(4)	0.018(3)
5.9	O_C(z0)	0.011(2)	0.3102(7)	0.646(3)	0.014(2)	O_C(zi)	0.516(2)	0.8290(7)	0.126(3)	0.015(2)
6.5		–0.003(3)	0.3095(8)	0.632(3)	0.014(2)		0.517(3)	0.8333(9)	0.122(3)	0.019(3)
7.8		0.010(3)	0.3083(9)	0.651(3)	0.011(3)		0.518(3)	0.8368(11)	0.120(4)	0.021(3)
5.9	O_D(00)	0.184(3)	0.1296(8)	0.195(3)	0.017(3)	O_D(0i)	0.675(3)	0.6540(10)	0.697(4)	0.028(3)
6.5		0.171(5)	0.1298(12)	0.181(5)	0.037(4)		0.681(6)	0.6603(14)	0.700(6)	0.047(5)
7.8		0.184(4)	0.1269(13)	0.198(5)	0.026(4)		0.654(7)	0.662(2)	0.681(9)	0.075(11)
5.9	O_D(z0)	0.195(3)	0.1187(8)	0.704(3)	0.019(3)	O_D(zi)	0.681(3)	0.6409(8)	0.192(3)	0.021(3)
6.5		0.188(4)	0.1162(9)	0.690(4)	0.022(3)		0.689(4)	0.6429(10)	0.204(4)	0.026(3)
7.8		0.192(3)	0.1141(10)	0.693(4)	0.015(3)		0.679(3)	0.6455(11)	0.192(4)	0.018(3)

All atoms except for Ba were refined with isotropic displacement parameters

The isotropic displacement exponent takes the form: $-8\pi^2 U(\sin\theta/\lambda)^2$

The coordinates of the $P2_1/c$ model have been reported without the ¼, ¼, ¼ origin shift to compare our data with other feldspar structures

[a] U_{eq} defined as one third of the trace of the orthogonalized U_{ij} tensor

parameters by the use of the Win_Strain4 program (Angel software 2011) up to 5.6 GPa (Table 5). In celsian, the main axis $\boldsymbol{\varepsilon_1}$ is only slightly more compressible than the others (46 % of the total strain) and, as in lead feldspar, the minor axis $\boldsymbol{\varepsilon_3}$ is parallel to **b** and the highest deformation occurs on the (010) plane, where $\boldsymbol{\varepsilon_1}$ and $\boldsymbol{\varepsilon_2}$ axes lie. In the plane,

Table 5 Linear axial compressibilities ($\times 10^{-3}$ GPa^{-1}), magnitudes ($\times -10^{-3}$ GPa^{-1}) and orientations of the principal axes of the strain ellipsoids for monoclinic *I*2/*c* feldspars in the *P* range 0.0001–8 GPa

	P range (GPa)	β_a	β_b	β_c		Unit strain	Angle with			$\varepsilon_1/(\varepsilon_1+\varepsilon_2+\varepsilon_3)$ (%)
							a	*b*	*c*	
$BaAl_2Si_2O_8$	0–5.6	5.65	3.14	4.02	ε_1	5.7(2)	5	90	119	46
This work					ε_2	3.6(1)	95	90	151	
					ε_3	3.2(1)	90	0	90	
$PbAl_2Si_2O_8$	0–7.7	5.57	3.12	4.72	ε_1	5.7	12	90	127	44
Curetti et al. (2015)					ε_2	4.3	78	90	37	
					ε_3	3.2	90	0	90	
$SrAl_2Si_2O_8$	0–6.6	4.40	3.64	4.35	ε_1	4.9	32	90	147	42
Pandolfo et al. (2011)					ε_2	3.7	90	0	90	
					ε_3	3.2	122	90	123	
$Ca_{0.2}Sr_{0.8}Al_2Si_2O_8$	4.2–7.1	4.63	3.93	4.88	ε_1	5.5	36	90	151	44
Nestola et al. (2004)					ε_2	4.0	90	0	90	
					ε_3	3.1	126	90	119	

The compressibilities were calculated as $\beta = -(d - d_0)/d_0 \times 1/P$, where d is a unit-cell parameter

The errors are ~0.01

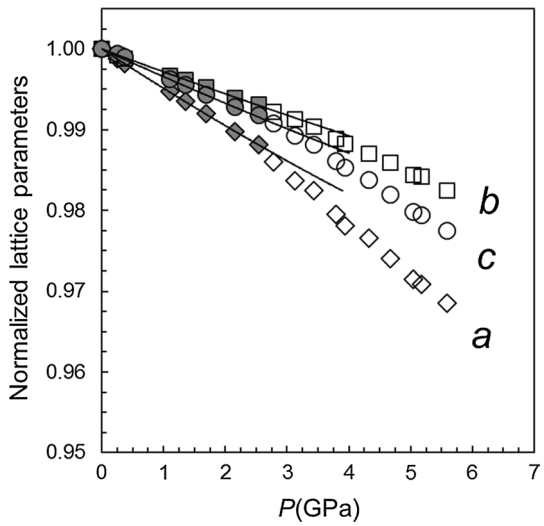

Fig. 3 Variation of the *a*, *b*, *c* unit-cell edges of celsian as a function of pressure, normalized to their room pressure values. *Diamonds*: a/a_0; *squares*: b/b_0; *circles*: c/c_0. *Lines* correspond to linear fits in the *P* range 0.0001–2.55 GPa (*gray symbols*) with linear moduli M_i = 197(1), 347(5), 285(4) GPa, respectively (with i = *a*, *b*, *c* and $M_i = \beta_i^{-1}$, Angel et al. 2014). *Open circles*: normalized parameters in the *P* range 2.79–5.59 GPa. Experimental uncertainties are smaller than *symbols*

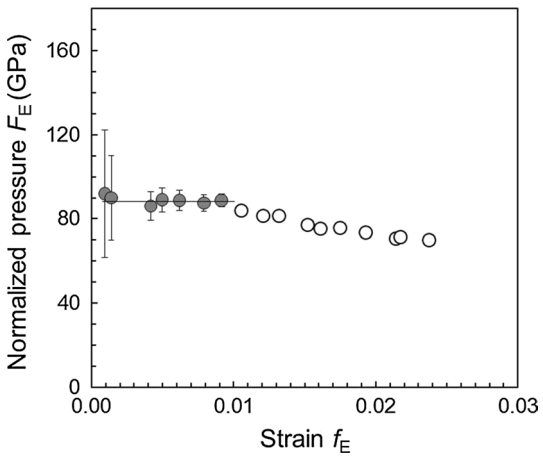

Fig. 4 Evolution of the normalized pressure F_E versus Eulerian finite strain f_E in celsian. $F_E = P/3 \times f_E \times (1 + 2\,f_E)^{5/2}$ and $f_E = [(V_o/V)^{2/3} - 1]/2$ (Angel 2000). The *horizontal line* of constant F_E indicates that the *P*–*V* data (*gray circles*, *P* range 0.0001–2.55 GPa) could be fitted by a second-order truncation of the BM-EoS. *Open circles*: *P*–*V* data in the *P* range 2.79–5.59 GPa

the main axis $\boldsymbol{\varepsilon_1}$ is oriented along a direction close to **a**. A comparison with the other feldspars studied at H*P* shows that in anorthite the maximum compression occurs close to the 001 plane with 70 % of the total strain along $\boldsymbol{\varepsilon_1}$ axis (Angel 1994) and in alkali feldspars some 55–65 % of the volume compression is accommodated by the linear compression close to **a***, which is then the direction of greatest compressibility (Angel et al. 1988, 2012; Angel 1994; Allan and Angel 1997; Nestola et al. 2008; Curetti et al. 2011).

As seen in the linear parameters behavior, also in the evolution of the unit-cell volume with pressure a slight change in the compressional behavior is observed for $P > 2.55$ GPa (Fig. 2). Consequently, the *P*–*V* data were fitted by a BM2-EoS only up to 2.55 GPa (*solid line* in figure) with the resulting EoS coefficients: $V_0 = 1461.4(1)$ Å^3 and $K_{T0} = 88.1$ (6) GPa. An attempt to fit the *P*–*V* data to a BM3-EoS or some other EoS did not provide any good

results. When our *P*–*V* data are reformulated as a normalized pressure—finite strain plot (F_E–f_E plot, Angel 2000), the values in the *P* range 0.0001–2.55 GPa lie on a horizontal line of constant F_E (indicating $K' = 4$) (Fig. 4), confirming that the data are adequately described by a BM2-EoS. Fitting the *P*–*V* data to a BM2-EoS in the *P* range 2.79–5.59 GPa gives a lower bulk modulus, 55.8(12) GPa, confirming the anomalous behavior of the volume values, that deflect from the BM2 curve for $P > 2.55$ GPa, indicating a pre-transition volume softening, precursor of the H*P* first-order phase transition at ~5.7 GPa. Using the facilities for the direct fitting of continuous phase transitions (Simplified Landau Model) of the 7.33/2016 version of EosFit7c software (Gonzalez-Platas et al. 2016), we have fitted the pre-transition elastic softening, obtaining the coefficients: $a_H = -6.0(2)$ and $\beta_H = 0.98(5)$, where a_H is the scaling parameters for the spontaneous strain arising from the H*P* phase transition and β_H is the exponents of the power-law term. The value of a_H, significantly different from zero, supports the pre-transition softening. As just seen, in celsian the volume softening occurs at $P > 2.55$ GPa, while in strontium feldspar it was observed at $P > 3.67$ GPa (Pandolfo et al. 2011) and in lead feldspar at $P > 4.27$ GPa (Curetti et al. 2015). Probably, the softening takes place in celsian at lower pressures than in strontium and lead feldspars because the pressure of the first-order transition is lower. The volume bulk modulus of celsian, 88.1(6) GPa, is similar to that of strontium feldspar (90 GPa), but higher than that of lead feldspar (76 GPa), and meaningfully higher than those reported for alkali feldspars (all on the range 50–60 GPa, Angel 1994).

The *I*2/*c*–*P*2$_1$/*c* phase transition

As seen before, at $P > 5.59$ GPa there is a discontinuity in the evolution of the unit-cell parameters (Fig. 1; Table 1), especially in the behavior of the *b* and β parameters, both decreasing very significantly. The discontinuity is also seen in the unit-cell volume versus pressure plot (Fig. 2). A similar discontinuity was observed in $An_{20}SrFsp_{80}$ feldspar at $P \sim 7.3$ GPa (Nestola et al. 2004), in strontium feldspar at $P \sim 6.6$ GPa (Pandolfo et al. 2011) and in lead feldspar at $P \sim 8$ GPa (Curetti et al. 2015), indicating the occurrence of a phase transition strongly first order in character. The discontinuities observed in celsian indicate the occurrence of an analogous first-order phase transition between 5.6 and 5.9 GPa. The appearance of *c*- and *d*-type reflections in the data collection at $P = 5.9$ GPa, the analysis of the systematic absence and the structural refinements at 5.9, 6.5 and 7.8 GPa (Table 2) indicate that the phase transition occurs from *I*2/*c* to *P*2$_1$/*c* symmetry. The scheme of intensity of the different reflections in *P*2$_1$/*c* celsian is $a > d > b \geq c$, in agreement with the results observed for *P*2$_1$/*c* $An_{20}SrFsp_{80}$ feldspar (Benna et al. 2007) and *P*2$_1$/*c* lead feldspar (Curetti et al. 2015).

Structural modifications

Structural results show that in the *P* range 0.0001–5.5 GPa the increase in pressure causes in *I*2/*c* celsian only minor modifications mainly involving shortening of the average ⟨Ba–O⟩ distances (Table 6) and variation in the T–O–T bond angles (Table 7). The coordination of Ba remains ninefold as in Newnham and Megaw (1960). The distances which decrease more are Ba–O_C, Ba–O_D and Ba–O_A(2). In particular, the O_C(0) oxygen that was the farthest at room pressure gradually approaches the Ba atom with increasing pressure (Table 6). Besides the Ba–O_A(2) distance, also the Ba–Ba distance along **a*** decreases significantly with pressure (Fig. 5a, b) and accounts for the overall decrease in the O_A(2)–Ba–Ba–O_A(2) distance, the "strut" of Megaw (1970). While the average ⟨T–O–T⟩ angle shows no change with increasing pressure, individual T–O–T angles show a variation, with some increasing and some decreasing, as typical for feldspars at H*P,* responding to pressure by tilting of essentially rigid tetrahedral (Angel 1994; Ross 2000; Angel et al. 2012, 2013). In celsian, the T_1(0)–O_C(0)–T_2(0) angle (the "hinge" of the crankshaft chains closing up in all feldspars according to Angel et al. 2005), significantly decreases to 122° at $P = 5.5$ GPa, while the T–O_D–T angles increase (Table 7). On the contrary, the T–O bond lengths and O–T–O angles do not change significantly.

The *I*2/*c*–*P*2$_1$/*c* transition at ~5.7 GPa involves a reduction in the symmetry with the loss of the twofold rotation axes and of one-half of the centers of symmetry. In the *P* lattice, the numbers of independent atomic sites are doubled and pairs of atoms related by the pseudo-body centering (**a** + **b** + **c**)/2 vector are present. Therefore, at $P = 5.9$ GPa (Fig. 5c, d) the single Ba-site that was present in *I*2/*c* space group is doubled in two independent Ba(0)- and Ba(*i*)-sites, which are no longer correlated by the center of symmetry. The configurations of the two independent Ba-sites show different shape, with changes in the coordination environment. In Ba(0)-polyhedron, the larger variation concerns the two O_C oxygen that are very close to Ba atom (Table 6) and move even closer to the cation with increasing pressure, while the Ba(0)–O_A(20) distance increases significantly with pressure from 2.61 to 2.80 Å, because the O_A(20) oxygen progressively moves away from the O_A(2)–Ba–Ba–O_A(2) alignment (Fig. 5d), and at $P = 7.8$ GPa forms an angle of about 20° with the "strut" direction. In the Ba(*i*)-polyhedron, the O_C(00) and O_C(z0) oxygens are further away and remain far with pressure, while the O_B(z0) approaches Ba atom. The O_A(20) oxygen too approaches dramatically Ba atom with increasing pressure [the Ba(*i*)–O_A(20) distance drops from 3.12 to 2.77 Å].

Table 6 Ba–O interatomic distances (Å) at different pressures

P (GPa)	0.0001	2.1	4.2	5.5
Space group	*I*2/*c*	*I*2/*c*	*I*2/*c*	*I*2/*c*
Ba–O_A(1)	2.808(13)	2.800(15)	2.744(18)	2.755(15)
Ba–O_A(1)	2.874(13)	2.831(14)	2.822(18)	2.800(15)
Ba–O_A(2)	2.649(16)	2.596(14)	2.539(17)	2.566(19)
Ba–O_B(0)	2.86(3)	2.89(2)	2.89(3)	2.84(4)
Ba–O_B(*z*)	2.95(3)	2.95(2)	2.89(3)	2.93(4)
Ba–O_C(0)	3.162(11)	3.119(11)	3.021(14)	3.003(16)
Ba–O_C(*z*)	3.076(12)	3.042(12)	2.983(15)	2.955(17)
Ba–O_D(0)	2.93(2)	2.86(2)	2.88(3)	2.85(3)
Ba–O_D(*z*)	2.93(2)	2.84(2)	2.84(3)	2.82(3)
⟨Ba–O⟩	2.92	2.88	2.84	2.84
P (GPa)	5.9	6.5	7.8	
Space group	$P2_1/c$	$P2_1/c$	$P2_1/c$	
Ba(0)–O_A(10)	2.818(15)	2.78(2)	2.750(19)	
Ba(0)–O_A(1*i*)	2.853(13)	2.84(2)	2.79(2)	
Ba(0)–O_A(20)	2.61(2)	2.67(3)	2.80(3)	
Ba(0)–O_A(2*i*)	3.32(3)	3.14(3)	3.19(4)	
Ba(0)–O_B(0*i*)	2.93(3)	2.86(4)	2.86(4)	
Ba(0)–O_B(*zi*)	2.84(3)	2.97(4)	2.97(4)	
Ba(0)–O_C(0*i*)	2.797(11)	2.733(14)	2.668(16)	
Ba(0)–O_C(*zi*)	2.811(14)	2.761(18)	2.72(2)	
Ba(0)–O_D(00)	2.85(2)	2.75(4)	2.82(4)	
Ba(0)–O_D(*z*0)	2.85(3)	2.72(3)	2.71(4)	
⟨Ba(0)–O⟩	2.87	2.82	2.83	
Ba(*i*)–OA(10)	2.758(17)	2.78(2)	2.77(2)	
Ba(*i*)–OA(1*i*)	2.724(15)	2.72(2)	2.74(3)	
Ba(*i*)–O_A(20)	3.12(4)	2.98(4)	2.77(4)	
Ba(*i*)–O_A(2*i*)	2.583(15)	2.54(2)	2.62(2)	
Ba(*i*)–O_B(00)	2.85(3)	2.79(4)	2.82(5)	
Ba(*i*)–O_B(*z*0)	2.93(3)	2.73(4)	2.78(4)	
Ba(*i*)–O_C(00)	3.085(13)	3.032(16)	3.045(19)	
Ba(*i*)–O_C(*z*0)	3.020(14)	2.941(16)	2.987(18)	
Ba(*i*)–O_D(0*i*)	2.92(3)	2.97(4)	2.94(6)	
Ba(*i*)–O_D(*zi*)	2.72(2)	2.81(3)	2.74(3)	
⟨Ba(*i*)–O⟩	2.87	2.83	2.82	

In Fig. 6, the M–M distances along **a*** direction are plotted versus pressure in different Al_2Si_2 feldspars for comparison. Figure 6a shows that in celsian the Ba–Ba distance along **a*** reaches the minimum value of 4.3 Å at $P = 5.5$ GPa in the *I*2/*c* configuration and after the transition stops to decrease and remains constant. Differently from what occurs in celsian, after the *I*2/*c*–$P2_1/c$ transition, the M–M distances along the "strut" in lead feldspar (Fig. 6b) and in $An_{20}SrFsp_{80}$ feldspar (Fig. 6c) significantly increase. In the two feldspars, the M–M distance along the "strut" reaches the maximum compression compatible within the *I*2/*c* symmetry with values (~3.9 Å) lower than that of the celsian, probably because of the smaller size of Ca, Sr and Pb cations with respect to Ba. Then, the transition to $P2_1/c$ allows in both the two feldspars a relaxation of the M–M distances while in celsian the Ba–Ba distance along **a*** is already large enough and no longer needs to increase.

In Fig. 7, the non-equivalent four-membered rings of tetrahedra, approximately normal to **a** direction, are projected on the $(\bar{1}\ 0\ 2)$ plane in the *I*2/*c* and $P2_1/c$ structures, respectively, at $P = 5.5$ GPa and at $P = 5.9$ GPa. In the *I*2/*c* configuration (Fig. 7a), there are two quite regular unique rings around the symmetry centers. The $T_1(0)$–$O_C(0)$–$T_2(0)$ and $T_1(z)$–$O_C(z)$–$T_2(z)$ are the smaller angles (Table 7).

Table 7 T–O–T angles (°) at different pressures

P (GPa)	0.0001	2.1	4.2	5.5		5.9	6.5	7.8
Space group	*I*2/*c*	*I*2/*c*	*I*2/*c*	*I*2/*c*		$P2_1/c$	$P2_1/c$	$P2_1/c$
$T_1(0)$–$O_A(1)$–$T_1(z)$	140.5(7)	139.6 (5)	138.9(7)	139.6(6)	$T_1(00)$–$O_A(10)$–$T_1(zi)$	140.3(8)	139.7(8)	139.1(10)
					$T_1(0i)$–$O_A(1i)$–$T_1(z0)$	139.0(7)	138.3(9)	136.6(11)
$T_2(0)$–$O_A(2)$–$T_2(z)$	136.2(13)	132.7(12)	134.9(13)	137.4(11)	$T_2(00)$–$O_A(20)$–$T_2(z0)$	133.3(8)	131.9(9)	127.2(16)
					$T_2(0i)$–$O_A(2i)$–$T_2(zi)$	134.7(17)	125(2)	136(3)
$T_1(0)$–$O_B(0)$–$T_2(0)$	146(2)	147.0(18)	148(3)	142(3)	$T_1(00)$–$O_B(00)$–$T_2(00)$	138.3(19)	135(3)	135(3)
					$T_1(0i)$–$O_B(0i)$–$T_2(0i)$	155(2)	148(3)	148(4)
$T_1(z)$–$O_B(z)$–$T_2(z)$	148(2)	148(2)	145(3)	146(3)	$T_1(z0)$–$O_B(z0)$–$T_2(z0)$	143(2)	130(2)	135(3)
					$T_1(zi)$–$O_B(zi)$–$T_2(zi)$	142(2)	153(3)	152(3)
$T_1(0)$–$O_C(0)$–$T_2(0)$	126.6(10)	125.4(9)	121.5(12)	121.9(13)	$T_1(00)$–$O_C(00)$–$T_2(0i)$	123.2(9)	119.7(12)	120.7(10)
					$T_1(0i)$–$O_C(0i)$–$T_2(00)$	113.6(12)	114.2(15)	109.7(17)
$T_1(z)$–$O_C(z)$–$T_2(z)$	128.7(9)	128.6(8)	128.1(8)	127.3(9)	$T_1(z0)$–$O_C(z0)$–$T_2(zi)$	124.0(7)	120.7(11)	122.7(8)
					$T_1(zi)$–$O_C(zi)$–$T_2(z0)$	126.1(10)	125.6(15)	124.3(17)
$T_1(0)$–$O_D(0)$–$T_2(0)$	139.3(12)	139.0(12)	144.3(16)	145(2)	$T_1(00)$–$O_D(00)$–$T_2(0i)$	141.1(13)	136(2)	141(3)
					$T_1(0i)$–$O_D(0i)$–$T_2(00)$	152.4(16)	153(2)	154(5)
$T_1(z)$–$O_D(z)$–$T_2(z)$	136.3(10)	137.1(12)	140.9(14)	143.0(18)	$T_1(z0)$–$O_D(z0)$–$T_2(zi)$	137.7(14)	129.5(18)	129(2)
					$T_1(zi)$–$O_D(zi)$–$T_2(z0)$	142.5(15)	150.2(17)	147(2)

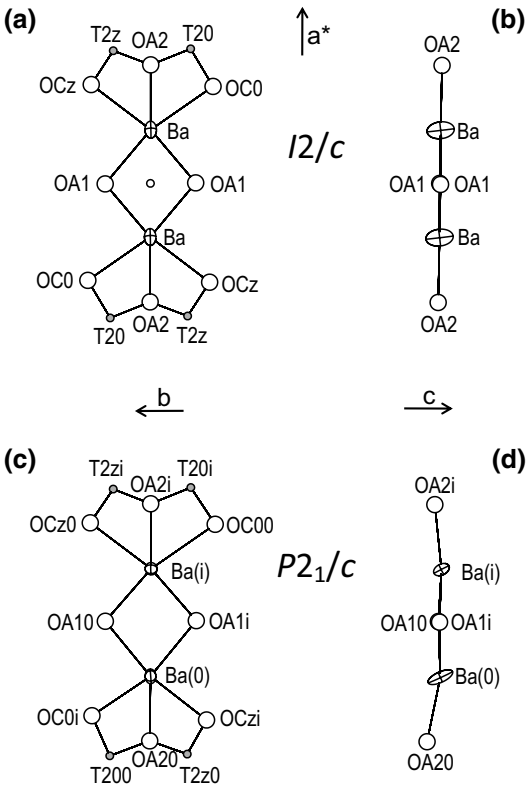

Fig. 5 Slices of the celsian structure elongated approximately parallel to **a***, before and after the $I2/c$–$P2_1/c$ phase transition, showing the $O_A(2)$–M–M–$O_A(2)$ "strut" that Megaw (1970) suggested hold the crankshaft chains extended. **a**, **c** View along **c** direction (thickness ~1.5 Å). **b**, **d** View along **b** direction (thickness ~5 Å). **a**, **b** *I*2/*c* configuration at $P = 5.5$ GPa; center of symmetry at ½, ½, 0. **c**, **d** $P2_1/c$ configuration at $P = 5.9$ GPa; the center of symmetry is lost

After the transition, in the $P2_1/c$ configuration (Fig. 7b), the higher flexing of the tetrahedral framework due to the increase in pressure causes greater differences between the four unique rings around the symmetry centers. The most distorted ring is the $T_1(0i)$–$T_2(00)$, in which the $T_1(0i)$–$O_C(0i)$–$T_2(00)$ angle is reduced to 114° (115° is often considered an extreme limit for Al–O–Si or Si–O–Si bonds, Benusa et al. 2005). The small value of this angle in celsian at H*P* is probably related to the remarkable modifications concerning O_C oxygens, as previously seen. An even more strong variation in the T–O_C–T angles was observed in $An_{20}SrFsp_{80}$ feldspar by Benna et al. (2007), with the extremely small value of 104°. The $I2/c$–$P2_1/c$ transition induces, besides the significant changes in the T–O–T bond angles, also a slight deformation of the internal O–T–O angles within the tetrahedra. The most deformed tetrahedra are the $T_2(00)$ and $T_1(zi)$ (Fig. 7b), with the $O_A(20)$–$T_2(00)$–$O_C(0i)$ angle of 96° and the $O_D(zi)$–$T_1(zi)$–$O_A(10)$ angle of 94°, respectively (Table 8, deposited of Electronic supplementary material).

Conclusion

As it is known, Al_2Si_2 feldspars (i.e., alkaline-earth and lead feldspars) show different symmetries with changes of pressure or composition: The $P\,\bar{1}$, $I\,\bar{1}$ and $I2/c$ space groups are observed at room and at low pressures, while the $P2_1/c$ phase is stable only at very high pressures. The space group of natural monoclinic barium feldspar (celsian) is $I2/c$. The present study demonstrates that in celsian too,

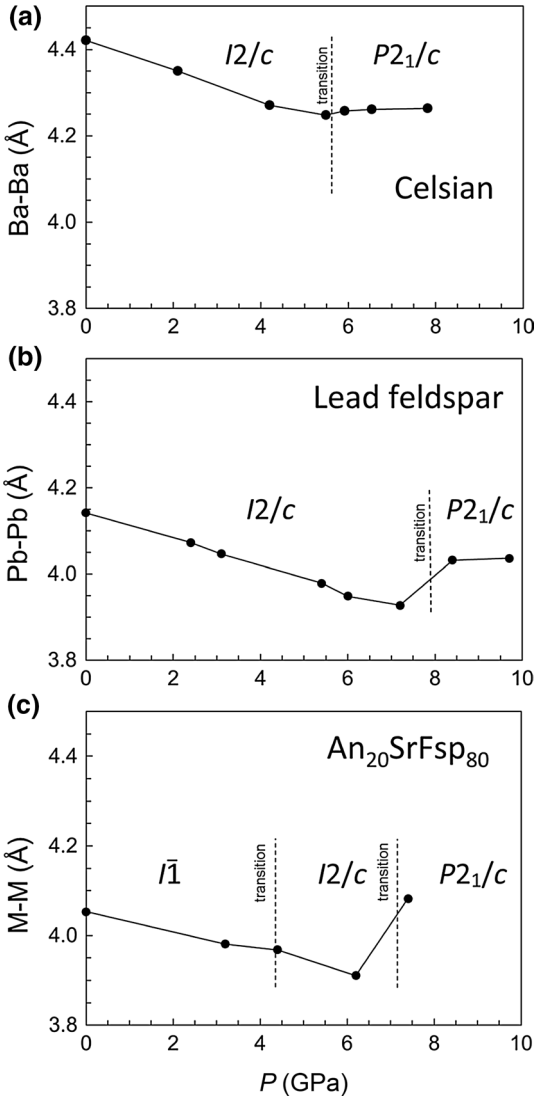

Fig. 6 Variation of the M–M distances along **a*** with pressure (**a**) celsian: the $I2/c$–$P2_1/c$ transition is at $P \sim 5.7$ GPa. **b** Lead feldspar: The $I2/c$–$P2_1/c$ transition is at ~8 GPa (Curetti et al. 2015). **c** $An_{20}SrFsp_{80}$ feldspar: The $I\bar{1}$–$I2/c$ triclinic–monoclinic transition is at ~4.3 GPa and the $I2/c$–$P2_1/c$ transition is at ~7.3 GPa (Benna et al. 2007). Experimental uncertainties are smaller than *symbols*

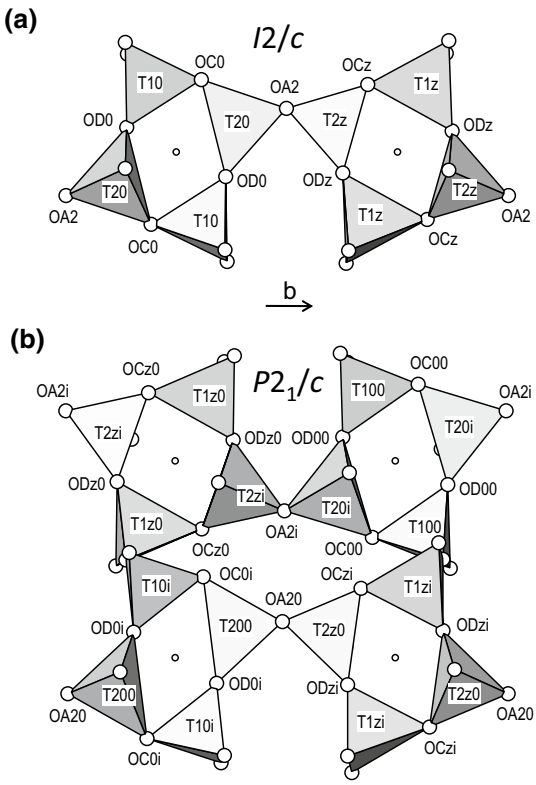

Fig. 7 Four-membered rings of tetrahedra around the symmetry centers, approximately normal to **a** direction, with ring planes near ($\bar{1}$ 0 2). Projection on ($\bar{1}$ 0 2) plane; the [$\bar{2}$ 0 $\bar{1}$] direction is vertical. $O_A(1)$ and O_B oxygen atoms are not labeled. **a** The two unique rings in $I2/c$ configuration at $P = 5.5$ GPa. Symmetry centers at ¼, ¼, ¼ and ¼, ¼, ¾. **b** The four unique rings in $P2_1/c$ configuration at $P = 5.9$ GPa. Centers at ½, 0, ½; ½, ½, ½; 0, 0, 0 and 0, ½, 0. The most distorted ring is the $T_1(0i)$–$T_2(00)$–$T_1(0i)$–$T_2(00)$, with the smallest $T_1(0i)$–$O_C(0i)$–$T_2(00)$ angle of 114°

at high pressure, there is the $I2/c$–$P2_1/c$ phase transition, as already observed in synthetic monoclinic $An_{20}SrFsp_{80}$, strontium and lead feldspars. In celsian, the $I2/c$–$P2_1/c$ transition occurs at ~5.7 GPa, a pressure lower than in strontium feldspar, in which the transition occurs at ~6.6 GPa (Pandolfo et al. 2011). The substitution of 20 % of $CaAl_2Si_2O_8$ component into the strontium feldspar structure (with a decrease in the mean ionic radius) causes a further increase in the transition pressure: in the $Ca_{0.2}Sr_{0.8}Al_2Si_2O_8$ feldspar the $I2/c$–$P2_1/c$ transition occurs at ~7.3 GPa (Nestola et al. 2004). Hence, the results obtained in the present work seem to confirm the possible correlation between the pressure of the $I2/c$–$P2_1/c$ transition and the size of the cation in the M-site in alkaline-earth feldspars (Curetti et al. 2015).

Acknowledgments Ross J. Angel is sincerely thanked for installing SINGLE software at Department of Earth Sciences, University of Torino, and for providing several software applications in his Web site. Reviews from two anonymous referees greatly improved the manuscript; we are grateful to them for critical reading and useful suggestions. The CrisDi and Scansetti Interdepartmental Centres of University of Torino are thanked. Financial support has been provided by "Ministero dell'Istruzione, dell'Università e della Ricerca" (MIUR), Roma.

References

Allan DR, Angel RJ (1997) A high-pressure structural study of microcline ($KAlSi_3O_8$) to 7 GPa. Eur J Mineral 9:263–275. doi:10.1127/ejm/9/2/0263

Angel RJ (1988) High-pressure structure of anorthite. Am Mineral 73:1114–1119

Angel RJ (1992) Order-disorder and the high-pressure $P\bar{1}$–$I\bar{1}$ transition in anorthite. Am Mineral 77:923–929

Angel RJ (1994) Feldspars at high pressure. In: Parsons I (ed) Feldspars and their reactions. Kluwer, Dordrecht, pp 271–312. doi:10.1007/978-94-011-1106-5_7

Angel RJ (2000) Equations of state. In: Hazen RM, Downs RT (eds) High-temperature and high-pressure crystal chemistry, vol 41, pp 35–59. Reviews in Mineralogy & Geochemistry, Mineralogical Society of America and Geochemical Society, Washington, DC. doi:10.2138/rmg.2000.41.2

Angel RJ, Finger LW (2011) SINGLE: a program to control single-crystal diffractometers. J Appl Crystallogr 44:247–251. doi:10.1107/S0021889810042305

Angel RJ, Gonzalez-Platas J (2013) ABSORB-7 and ABSORB-GUI for single-crystal absorption corrections. J Appl Crystallogr 46:252–254. doi:10.1107/S0021889812048431

Angel RJ, Hazen RM, McCormick TC, Prewitt CT, Smyth JR (1988) Comparative compressibility of end-member feldspars. Phys Chem Miner 15:313–318. doi:10.1007/BF00311034

Angel RJ, Carpenter MA, Finger LW (1990) Structural variation associated with compositional variation and order-disorder behavior in anorthite-rich feldspars. Am Mineral 75:150–162

Angel RJ, Allan DR, Miletich R, Finger LW (1997) The use of quartz as an internal pressure standard in high pressure crystallography. J Appl Crystallogr 30:461–466. doi:10.1107/S0021889897000861

Angel RJ, Downs RT, Finger LW (2000) High-temperature—high-pressure diffractometry. In: Hazen RM, Downs RT (eds) High-temperature and high-pressure crystal chemistry, vol 41, pp 559–596. Reviews in Mineralogy & Geochemistry, Mineralogical Society of America and Geochemical Society, Washington, DC. doi:10.2138/rmg.2000.41.16

Angel RJ, Ross NL, Zhao J (2005) The compression of framework minerals: beyond rigid polyhedra. Eur J Mineral 17:193–199. doi:10.1127/0935-1221/2005/0017-0193

Angel RJ, Sochalski-Kolbus LM, Tribaudino M (2012) Tilts and tetrahedra: the origin of the anisotropy of feldspars. Am Mineral 97:765–778. doi:10.2138/am.2012.4011

Angel RJ, Ross NL, Zhao J, Sochalski-Kolbus L, Krüger H, Schmidt BC (2013) Structural controls on the anisotropy of tetrahedral frameworks: the example of monoclinic feldspars. Eur J Mineral 25:597–614. doi:10.1127/0935-1221/2013/0025-2323

Angel RJ, Gonzalez-Platas J, Alvaro M (2014) EosFit7c and a Fortran module (library) for equation of state calculations. Z Kristallogr 229:405–419. doi:10.1515/zkri-2013-1711

Benna P, Nestola F, Boffa Ballaran T, Balić-Žunić T, Fahl Lundegaard L, Bruno E (2007) The high-pressure structural configurations of $Ca_{0.2}Sr_{0.8}Al_2Si_2O_8$ feldspar: the $I\bar{1}$–$I2/c$ and $I2/c$–$P2_1/c$ phase transitions. Am Mineral 92:1190–1199. doi:10.2138/am.2007.2402

Benusa MD, Angel RJ, Ross NL (2005) Compression of albite $NaAlSi_3O_8$. Am Mineral 90:1115–1120. doi:10.2138/am.2005.1805

Curetti N, Sochalski-Kolbus L, Angel RJ, Benna P, Nestola F, Bruno E (2011) High-pressure structural evolution and equation of state of analbite. Am Mineral 96:383–392. doi:10.2138/am.2011.3604

Curetti N, Benna P, Bruno E (2015) High-pressure equation of state and phase transition in $PbAl_2Si_2O_8$ feldspar. Am Mineral 100:1568–1577. doi:10.2138/am-2015-5000

Downs RT, Hazen RM, Finger LW (1994) The high pressure crystal chemistry of low albite and the origin of the pressure dependency of Al–Si ordering. Am Mineral 79:1042–1052

Gonzalez-Platas J, Alvaro M, Nestola F, Angel R (2016) EosFit7-GUI: a new graphical user interface for equation of state calculations, analyses and teaching. J Appl Crystallogr 49:1377–1382. doi:10.1107/S1600576716008050

Griffen DT, Ribbe PH (1976) Refinement of the crystal structure of celsian. Am Mineral 61:414–418

King HE, Finger LW (1979) Diffracted beam crystal centering and its application to high pressure crystallography. J Appl Crystallogr 12:374–378. doi:10.1107/S0021889879012723

Mao HK, Xu J, Bell PM (1986) Calibration of the ruby pressure gauge to 800 kbar under quasi-hydrostatic conditions. J Geophys Res 9:4673–4676. doi:10.1029/JB091iB05p04673

Megaw HD (1970) Structural relationship between coesite and feldspars. Acta Cryst B26:261–265. doi:10.1107/S0567740870002236

Miletich R, Allan DR, Kuhs WF (2000) High-pressure single-crystal techniques. In: Hazen RM, Downs RT (eds) High-temperature and high-pressure crystal chemistry, vol 41, pp 445–520. Reviews in Mineralogy & Geochemistry, Mineralogical Society of America and Geochemical Society, Washington, DC. doi:10.2138/rmg.2000.41.14

Miletich R, Gatta GD, Willi T, Mirwald PW, Lotti P, Merlini M, Rotiroti N, Loerting T (2014) Cordierite under hydrostatic compression: Anomalous elastic behavior as a precursor for a pressure-induced phase transition. Am Mineral 99:479–493. doi:10.2138/am.2014.4487

Nestola F, Boffa Ballaran T, Benna P, Tribaudino M, Bruno E (2004) High-pressure phase transitions in $Ca_{0.2}Sr_{0.8}Al_2Si_2O_8$ feldspar. Am Mineral 89:1474–1479. doi:10.2138/am-2004-1015

Nestola F, Curetti N, Benna P, Ivaldi G, Angel RJ, Bruno E (2008) Compressibility and high-pressure behavior of $Ab_{63}Or_{27}An_{10}$ anorthoclase. Can Mineral 46:1443–1454. doi:10.3749/canmin.46.6.1443

Newnham RE, Megaw HD (1960) The crystal structure of celsian (barium feldspar). Acta Cryst 13:303–312. doi:10.1107/S0365110X60000765

North ACT, Phillips DC, Mathews FS (1968) A semi-empirical method of absorption correction. Acta Cryst A24:351–359. doi:10.1107/S0567739468000707

Pandolfo F, Ballaran TB, Nestola F, Muller MK, Mrosko M, Bruno E (2011) High-pressure $I2/c$–$P2_1/c$ phase transformation in $SrAl_2Si_2O_8$ feldspar. Am Mineral 96:1182–1185. doi:10.2138/am.2011.3797

Ross NL (2000) Framework structures. In: Hazen RM, Downs RT (eds) High-temperature and high-pressure crystal chemistry, vol 41, pp 257–287. Reviews in Mineralogy & Geochemistry, Mineralogical Society of America and Geochemical Society, Washington, DC. doi:10.2138/rmg.2000.41.9

Sheldrick GM (2008) A short history of SHELX. Acta Cryst A64:112–122. doi:10.1107/S0108767307043930

Tribaudino M, Benna P, Bruno E, Hanfland M (1999) High pressure behaviour of lead feldspar ($PbAl_2Si_2O_8$). Phys Chem Miner 26:367–374. doi:10.1007/s002690050196